



Interplay of Electrode Heterogeneity and Lithium Plating

Amir-Sina Hamed,*,^{1b} Fezfeh Pouraghajan, Fei Sun, Mojdeh Nikpour,^{1b} and Dean R. Wheeler*,^z

Chemical Engineering Department, Brigham Young University, Provo, Utah

Lateral microstructure heterogeneity in anodes is known to induce nonuniform current density, state of charge, and lithium plating. This means that such electrode heterogeneity can limit the fast charging of lithium-ion batteries. In this work, a combination of experiments and simulation is employed to understand the effect of mm scale lateral heterogeneity on cell aging. A previously developed model was extended to efficiently simulate SEI formation and Li plating for independent regions of an electrode. The model consists of three parallel regions each described under a P2D framework and with a distinct ionic resistance and possibly active material loading. The results suggest that during fast charge when the active material is uniformly distributed across the three regions, the region with the highest resistance reaches the end of life sooner than the other regions. There is also positive feedback from Li metal filling the pores near the separator interface that further accelerates lithium plating. Finally, when there is a non-uniform active material distribution associated with the ionic resistance heterogeneity, tight competition between regions can occur, leading to less overall lithium plating and plating that is more uniform between regions.

© 2022 The Electrochemical Society ("ECS"). Published on behalf of ECS by IOP Publishing Limited. [DOI: 10.1149/1945-7111/ac5304]

Manuscript submitted December 20, 2021; revised manuscript received February 3, 2022. Published February 17, 2022.

Battery degradation remains a challenge toward further improvement of Li-ion batteries, especially for electric vehicle applications that require long cycle life, high-rate charging, and tolerance for a wide range of operating temperatures. Among the different mechanisms of cell aging, solid electrolyte interphase (SEI) growth and lithium plating on the anode are considered two of the main contributors to capacity fade due to the loss of active lithium.¹⁻⁴

Organic electrolytes that are commonly used in Li-ion batteries are thermodynamically unstable at the wide operating potential of the batteries. Hence, during the first few cycles, the electrolyte undergoes a reduction reaction at the interface of the negative electrode. As a result, a passivating layer composed of organic and inorganic decomposition products forms at the electrode/electrolyte interface, i.e. the SEI. This layer should ideally be an insulator for electrons while allowing lithium ions to pass through it. As this layer grows, it becomes self-inhibiting to further growth, making long-term operation of the battery possible.⁵⁻⁹

Formation and progressive growth of the SEI layer depend on the nature of graphite, electrolyte, additives, and operating conditions. Lower anode potentials and high temperatures can lead to faster growth of the SEI layer.¹⁰ An irreversible capacity loss due to SEI formation could be on the order of 10% during the formation cycles.⁹ Furthermore, when the current is flowing there will be a voltage drop across the SEI. This ohmic loss in addition to the diffusional resistance will increase with SEI thickness.

Lithium plating is another phenomenon that contributes to capacity fade. Lithium plating can occur at the surface of the anode at potentials below 0 V vs Li/Li+. Such anode polarization to low potentials can be caused by a combination of ohmic potential drop, charge transfer overpotential, and diffusion overpotential.² The lithium plating reaction can take place in parallel to intercalation on the negative electrode during cell charging. Some portion of the plated lithium is reversible and can be stripped in a subsequent discharge or during a rest period¹¹ when the relaxation in overpotentials causes it to be thermodynamically favorable to ionize again. Such reversible lithium is not harmful by itself to cell capacity. However, a portion of the plated lithium will react with electrolyte and form a new SEI layer, or can eventually become electronically isolated, in either case contributing to a loss of active lithium and thus cell capacity.²

Furthermore, significant lithium plating can pose safety problems. If lithium deposition grows dendritically, it may pierce the separator and cause an internal short.¹² Moreover, the presence of

lithium metal can increase the risk of exothermic reaction with electrolyte.² Therefore, it is crucial to mitigate this issue.

Charging at a low temperature or high rate or attempting to exceed charging capacity can exacerbate the rate of lithium plating. However, lithium plating is not limited to these conditions; other factors such as the nature of the electrolyte, anode/cathode capacity ratio, and manufacturing defects also have an impact on the lithium plating process.^{6,13-15}

Another factor that can play a significant role in battery degradation is microscale inhomogeneities.¹⁶ For commercial Li-ion-battery electrodes, active materials, carbon particles, binders, and pores are not uniformly distributed throughout the volume of the film. Non-uniform distribution of particles in addition to particle size and shape distribution leads to an inhomogeneous microstructure at the mm length scale. This can cause conductivity and local current density variations, leading to faster degradation, and prevent optimal utilization of the electrodes.¹⁷⁻²⁰

Although battery models can successfully predict routine battery performance, predicting failure and degradation during high-rate charge and discharge is still a challenge. Even highly detailed battery models routinely assume that electrodes are macro-homogeneous and isotropic; however, even well-made commercial electrodes are not necessarily homogeneous or isotropic. For example, Kerwald et al.²¹ reported a factor of three in local tortuosity variability, which means the local charging and discharging rate can deviate substantially from the mean. Other work has likewise quantified Li-ion battery electrode anisotropy and inhomogeneity based on a combination of X-ray imaging and image-based simulations.^{16,22-25}

Electrode microstructural heterogeneity, especially tortuosity variation, can specifically lead to metallic lithium plating. The variation in local current density leads to a non-uniform state of charge (SOC), which means parts of the electrodes get locally overcharged contributing to lithium deposition.²⁶

Despite the significant contribution of microstructural heterogeneity to battery degradation, it has not been accounted for in battery macro-homogeneous models that are widely used for predicting battery failure and degradation.²⁷⁻³⁰ Including such microstructural details in the model can make it numerically very expensive to run, especially as a full 3D model. For instance, if the heterogeneity exists on an mm length scale, then a 3D simulation of a volume large enough to accommodate this heterogeneity would be extremely computationally demanding. Therefore, it is advantageous to develop an approach to include electrode heterogeneity without implementing a full 3D model.

Prior work in our group used a computationally effective tool that was a combination of a Newman-type P2D model and an equivalent-

*Electrochemical Society Member.

^zE-mail: dean_wheeler@byu.edu

circuit sub-model to study the effect of electrode heterogeneity on cell performance.³¹ In this model, three regions with different microstructural properties across the electrodes were operating in parallel and only communicating electronically through current collectors. This parallel-heterogeneity approach is reasonable as long as heterogeneities in the lateral direction (across the surface of the electrode film) take place on larger distance scales than the thickness of the film, which appears to be the case based on the experimental determination of heterogeneity.³²

Different types of electrode heterogeneities, in terms of non-uniform ionic resistance and active material loading, were studied at different rates of discharge and charge. The result showed heterogeneity, especially at high-rate charging, can lead to non-uniform temperature, current density, positive and negative electrode states of charge. Such non-uniformities are known to adversely affect cell lifetime.^{16,33} Applying this principle locally means there could be a premature failure in some regions of the cell.

To further demonstrate the impact of electrode heterogeneity on cell degradation, in the present work we extend the prior model to account for SEI formation and lithium plating side reactions. Another modification to the previous model is considering thermal equilibration through the current collector. For the modified model, the parameters were measured or estimated for an NCA/graphite cell and validated with experiments on a commercial 18650 cell and associated coin cell and pouch cell cycling data. Electrodes were harvested from the 18650 cell and reassembled in pouch and coin cells.

In order to mitigate Li plating in a cell, it is necessary to understand the root causes of this degradation mode. The purpose of this work is to demonstrate the degree that local lithium plating observed on the surface of a cycled cell is related to the local structural heterogeneity in the electrode. In this work, we designed a simulation to better understand the relationship between electrode heterogeneity and Li plating. We investigated whether anode or cathode heterogeneity influences Li plating in a cell; also, whether there is any feedback mechanism or interplay between electrode heterogeneity and Li plating with cell cycling.

In the remainder of this paper, two sections discuss different parts of the electrochemical P2D-based model. This is followed by an experimental section for the different electrochemical cells that were

cycled at high C-rate charging to intentionally form lithium deposits. Finally, there is a discussion section that includes the model parameterization and validation followed by an explanation of the observed effects of electrode heterogeneity on localized Li plating.

Model Description

In this work, we again use a parallel-region model to model heterogeneity.³¹ Each of the three P2D electrochemical models has the same physical equations but, in some instances, different parameters to represent local variations. The base model is based on the model developed by Doyle and Newman, which uses a porous electrode and concentrated solution theories.^{34,35} To incorporate the Li-plating reaction, we use the model proposed by Arora³⁶ and for the SEI reaction, a model proposed by Yang et al.²⁸ that is based on the diffusion-limited SEI model by Safari et al.³⁷

Present Li deposition models can be categorized into two groups. The first group^{29,30,36,38} considers Li deposition as a reversible reaction that allows for plating and stripping reactions with generally asymmetric cathodic and anodic transfer coefficients (e.g., $\alpha_c = 0.7$ and $\alpha_a = 0.3$). A reversible reaction means that Li deposits can dissolve during rest and discharge. The amount of reversibility can be further tuned by adding a correction term to the Butler-Volmer equation. A subset of this group^{39,40} recently considered lithium metal activity as a function of Li-plating coverage on the surface of particles. Furthermore, they added chemical intercalation as a parallel reaction to lithium stripping.

In our experience attempting to use a reversible (even if asymmetric) plating model, all the plated lithium is stripped during subsequent cycles due to natural electrochemical driving forces. This means that so-called dead lithium does not accumulate from cycle to cycle, and no cell degradation is observed over long-term cycling. The only way to overcome this is to add a second and irreversible reaction, or otherwise modify the Butler-Volmer kinetic expression for forming lithium metal.⁴¹

The second main group of Li deposition models neglects the stripping part of the reaction and considers irreversible Li plating as its own reaction. For an irreversible plating reaction, one of two approximations is used: either a cathodic Tafel expression^{27,28} or a standard Butler-Volmer reaction,^{42,43} which is made asymmetric by

Table I. Baseline model parameters obtained from other works^{31,38,43} or from our experiments (*) as indicated.

Symbol	Description	Unit	Negative electrode	Separator	Positive electrode
L_i	Thickness	μm	48 *	25 *	36 *
$R_{p,i}$	Particle radius	μm	10.5	—	4.6
ϵ_i	Porosity	—	0.34 *	0.45	0.243 *
$\epsilon_{f,i}$	Filler fraction	—	0.055 *	—	0.079 *
ρ_i	Density	kg m^{-3}	2500	1100	2500
$C_{p,i}$	Specific heat	$\text{J kg}^{-1} \text{K}^{-1}$	700	700	700
λ_i	Thermal conductivity	$\text{W m}^{-1} \text{K}^{-1}$	1.7	0.16	2.1
σ_i	Electronic conductivity	S m^{-1}	46.1 *	—	16.2 *
D_i^s	Solid-phase diffusivity	$\text{m}^2 \text{s}^{-1}$	$5 \times 10^{-14} *$	—	$3 \times 10^{-13} *$
c_s^{max}	Maximum solid-phase concentration	mol m^{-3}	31370	—	51385
c_e^{init}	Initial electrolyte-phase concentration	mol m^{-3}	1000	1000	1000
$i_{0,\text{ref}}^{\text{int}}$	Exchange current density for intercalation reaction	A m^{-2}	1.44 *	—	1.57 *
E_a^{int}	Activation energy of intercalation reaction	J mol^{-1}	4.5×10^4	—	3.5×10^4
$E_a^{D_s}$	Solid-phase diffusion activation energy	J mol^{-1}	4×10^4	—	3×10^4
α_{int}	Transfer coefficient for intercalation	—	0.5	—	0.5
F	Faraday's constant	C mol^{-1}	—	96485	—
R	universal gas constant	$\text{J mol}^{-1} \text{K}^{-1}$	—	8.314	—
t^+	Cation transference number	—	—	0.38	—
T_{ref}	Reference temperature	K	—	297.15 *	—
T_{∞}	Ambient temperature	K	—	298.15	—
h	Heat transfer coefficient	$\text{W m}^{-2} \text{K}$	—	1	—

truncating the stripping current to zero when the overpotential is positive. In this work, we adopt the latter form of irreversible Li plating. For simplicity, we assume that any reversible part of the Li-plating reaction can be lumped into the negative electrode intercalation reaction, although there is a slight difference in their reaction potentials. Essentially, the reversible plating/stripping of lithium in a cell is for our purposes indistinguishable from regular graphite lithium intercalation. It is not well-known what fraction of the Li is reversible. In a sense, we circumvent the issue by assuming that the reversible Li does not need to be separately dealt with and only explicitly model the irreversible part.

The baseline model parameters are summarized in Table I. Parameters are principally based on our measurements for a commercial 18650 NCA/graphite cell. Some parameters are obtained or estimated from the literature as referenced.

The equations for calculating effective electrolyte diffusivity and conductivity, effective solid diffusivity and conductivity, and activity coefficient are obtained from reference [31]. Table II provides parameters used in side reaction models.

Table III lists structural parameters (tortuosity, porosity) of three characteristic electrode regions with low, middle, and high ionic resistances. In this table, ϵ_N stands for electrolyte volume fraction inside electrodes, N_M for MacMullin Number, and ϵ_f is the volume fraction of the solid additives (e.g., carbon black and binder). The medium region parameters are the same as the base model where τ , ϵ and N_M are obtained through measurements. The tortuosity values for the low and high regions were chosen as $\pm 20\%$ of the medium region tortuosity. The rest of the parameters of the other regions were changed in a way that the percentage of the active material remains constant in all three regions.

Governing equations and boundary conditions.—The parallel P2D models each follow a fairly traditional set of equations that are included here for completeness and also to show how SEI formation and Li plating fit into the remainder of the model.

Material balance equations.—Li-ion diffusion inside the solid active particles is described by Fick's second law in spherical coordinates:

$$\frac{\partial c_{s,i}}{\partial t} = \frac{1}{r^2} \frac{\partial}{\partial r} \left(D_{\text{eff},i}^s r^2 \frac{\partial c_{s,i}}{\partial r} \right) \quad [1]$$

where $c_{s,i}$ is the solid phase concentration of Li in the respective positive (P) and negative (N) active particle ($i = N$ or P) and $D_{\text{eff},i}^s$ is the effective solid-phase diffusion coefficient, which is a function

of temperature and solid-phase concentration. Li^+ flux is zero at the center of the particle and the flux at the surface of the particle ($r = R$) is defined based on the current density of the electrochemical reaction

$$-D_{s,i} \frac{\partial c_{s,i}}{\partial r} \Big|_{r=0} = 0 \quad [2]$$

$$-D_{s,i} \frac{\partial c_{s,i}}{\partial r} \Big|_{r=R} = j_i \quad [3]$$

Li^+ transport in the electrolyte phase is considered 1D only in the x -direction (normal to the current collector). The electrolyte-phase material balance is described by

$$\epsilon_i \frac{\partial c_{e,i}}{\partial t} = \frac{\partial}{\partial x} \left(D_{\text{eff},i} \frac{\partial c_{e,i}}{\partial x} \right) + j_i a_i (1 - t^+) \quad [4]$$

where $c_{e,i}$ is the electrolyte concentration distribution in the positive or negative active particle or separator ($i = P, N$ or S) and $D_{\text{eff},i}$ is the effective electrolyte-phase diffusion coefficient, which is a function of temperature and electrolyte concentration. j_i is the pore-wall flux defined in Eq. 24 for the negative electrode and Eq. 25 for the positive electrode. In the separator, there is no electrochemical reaction and therefore j_S is zero. ϵ_i is electrolyte volume fraction and a_i is the specific interfacial area of the particles per unit volume of the electrode, defined as

$$a_i = \frac{3(1 - \epsilon_i - \epsilon_{f,i})}{R_{p,i}} \quad [5]$$

where $R_{p,i}$ is the radius of active particles, and $\epsilon_{f,i}$ is the volume fraction of filler (carbon and binder). Spherical active particles with uniform size are assumed. The flux of Li^+ in the electrolyte phase is set to zero at both external boundaries (current collectors).

$$-D_{\text{eff},N} \frac{\partial c_{e,N}}{\partial x} \Big|_{x=0} = 0 \quad [6]$$

$$-D_{\text{eff},P} \frac{\partial c_{e,P}}{\partial x} \Big|_{x=L_N+L_S+L_P} = 0 \quad [7]$$

Continuous flux is considered for Li^+ at internal boundaries (i.e., $x = L_N, L_N + L_S$).

Table II. Parameters used for the Li plating and SEI reactions obtained from other works^{27,28,43} or from our experiments (*) as indicated.

Symbol	Description	Unit	Value
U_{Li}	Equilibrium potential of Li plating	V	0
$i_{0,\text{ref}}^{\text{Li}}$	Exchange current density of Li plating (coin cell)	A m ⁻²	9.6 *
E_a^{Li}	Activation energy of Li plating reaction	J mol ⁻¹	6.8×10^4
α_{Li}	Transfer coefficient of Li plating	—	0.3, 0.7
M_{Li}	Molecular mass of lithium	kg mol ⁻¹	6.94×10^{-3}
ρ_{Li}	Density of lithium	kg m ⁻³	534
U_{SEI}	Equilibrium potential of SEI formation	V	0.4
$k_{0,\text{ref}}^{\text{SEI}}$	Rate constant of SEI formation	m s ⁻¹	1.5×10^{-16} *
E_a^{SEI}	Activation energy of SEI formation	J mol ⁻¹	3×10^4
α_{SEI}	Transfer coefficient of SEI formation	—	0.5
σ_{SEI}	Electronic conductivity of SEI film	S m ⁻¹	5×10^{-6}
M_{SEI}	Molecular mass of SEI	kg mol ⁻¹	0.162
ρ_{SEI}	Density of SEI film	kg m ⁻³	1690
C_{EC}^0	Bulk concentration of EC	mol m ⁻³	4541
D_{EC}	EC diffusivity	m ² s ⁻¹	2×10^{-18}

Table III. The anode and cathode parameters for three regions with different ionic resistances.

Parameter		Low region	Medium region	High region
Negative electrode	ϵ_N	0.36	0.34	0.32
	ϵ_f	0.035	0.055	0.075
	τ_N	4.4	5.5	6.6
	N_M	12.2	16.2	20.6
Positive electrode	ϵ_P	0.263	0.243	0.223
	ϵ_f	0.059	0.079	0.099
	τ_P	1.9	2.3	2.8
	N_M	7.1	9.6	12.5

Charge balance equations.—Charge balance in the solid phase is expressed as

$$\sigma_{\text{eff},i} \frac{\partial^2 \varphi_{s,i}}{\partial x^2} = j_i a_i F \quad [8]$$

where $\sigma_{\text{eff},i}$ is the effective electronic conductivity in the solid phase, $\varphi_{s,i}$ is solid-phase potential, and F is Faraday's constant. At the anode side, the current collector is grounded while at the cathode side, the electronic charge flux is taken to be equal to the applied current density I_{app} , while there is no electronic current at the two internal boundaries with the separator:

$$\varphi_{s,N}|_{x=0} = 0, \quad \sigma_{\text{eff},i} \frac{\partial \varphi_{s,P}}{\partial x} \Big|_{x=L_N+L_S+L_P} = -I_{\text{app}} \quad [9]$$

$$\sigma_{\text{eff},i} \frac{\partial \varphi_{s,i}}{\partial x} \Big|_{x=L_N, L_N+L_S} = 0 \quad [10]$$

The cell voltage is set between the two current collectors:

$$V_{\text{cell}} = \varphi_{s,P}|_{x=L_N+L_S+L_P} - \varphi_{s,N}|_{x=0} \quad [11]$$

The electrolyte phase potential distribution is given by

$$\begin{aligned} -\frac{\partial}{\partial x} \left(k_{\text{eff},i} \frac{\partial \varphi_{e,i}}{\partial x} \right) + \frac{2RT}{F} (1-t^+) \left(1 + \frac{\partial \ln f_{\pm,i}}{\partial \ln c_{e,i}} \right) \\ \times \frac{\partial}{\partial x} \left(k_{\text{eff},i} \frac{\partial \ln c_{e,i}}{\partial x} \right) = j_i a_i F \end{aligned} \quad [12]$$

where $k_{\text{eff},i}$ is the effective ionic conductivity in the electrolyte phase, $\varphi_{e,i}$ is electrolyte-phase potential, R is the gas constant. The electrolyte phase current is set to be zero at the current collectors:

$$-k_{\text{eff},i} \frac{\partial \varphi_{e,i}}{\partial x} \Big|_{x=0, L_N+L_S+L_P} = 0 \quad [13]$$

Energy balance equation.—Energy conservation used in our model determines the temperature and follows the thermal model described by Gu et al.⁴⁴

$$\rho_i C_{p,i} \frac{\partial T}{\partial t} = \lambda_i \frac{\partial^2 T}{\partial x^2} + Q_{\text{rxn},i} + Q_{\text{ohm},i} + Q_{\text{rev},i} \quad [14]$$

where T is the temperature and ρ , C_p , and λ are the volume-averaged density, specific heat, and thermal conductivity respectively. The total reaction heat generation rate $Q_{\text{rxn},i}$ is defined as

$$Q_{\text{rxn},i} = j_i a_i F \eta_i \quad [15]$$

The total ohmic heat generation rate $Q_{\text{ohm},i}$ is defined as

$$\begin{aligned} Q_{\text{ohm},i} = \sigma_{\text{eff},i} \left(\frac{\partial \varphi_{s,i}}{\partial x} \right)^2 + k_{\text{eff},i} \left(\frac{\partial \varphi_{e,i}}{\partial x} \right)^2 \\ + k_{\text{eff},i} \frac{2RT_i}{F} (1-t^+) \left(1 + \frac{\partial \ln f_{\pm,i}}{\partial \ln c_{e,i}} \right) \frac{\partial \ln c_{e,i}}{\partial x} \frac{\partial \varphi_{e,i}}{\partial x} \end{aligned} \quad [16]$$

The total reversible heat generation rate $Q_{\text{rev},i}$ is defined as

$$Q_{\text{rev},i} = j_i a_i F T_i \frac{\partial U_i}{\partial T} \Big|_{T_{\text{ref}}} \quad [17]$$

It is not experimentally possible to separate the reversible heat generation for two electrodes, but it is immaterial because in this model the whole system is effectively at the same temperature at a given time. Note that $Q_{\text{rev},i}$ and $Q_{\text{rxn},i}$ are zero for the separator. For simplicity the boundary conditions at the current collectors are given by Newton's law of cooling:

$$-N \frac{\partial T_N}{\partial x} \Big|_{x=0} = h(T_{\infty} - T_N) \quad [18]$$

$$-P \frac{\partial T_P}{\partial x} \Big|_{x=L_N+L_S+L_P} = h(T_P - T_{\infty}) \quad [19]$$

where T_{∞} is the ambient temperature and h is a heat transfer coefficient meant to approximately capture all the mechanisms of heat exchange between the cell and the environment. Heat flux and temperature are continuous on the internal boundaries.

Electrochemical kinetic equations.—The rate of intercalation at the surface of the particle is governed by the Butler-Volmer equation:

$$j_{\text{int},i} = \frac{i_{0,\text{int},i}}{F} \left[\exp \left(\frac{\alpha_{a,\text{int}} F \eta_{\text{int},i}}{RT} \right) - \exp \left(-\frac{\alpha_{c,\text{int}} F \eta_{\text{int},i}}{RT} \right) \right] \quad [20]$$

where $\alpha_{a,\text{int}}$ and $\alpha_{c,\text{int}}$ are transfer coefficients for the reaction. The exchange current density, $i_{0,\text{int},i}$, has both temperature and concentration dependence as given by

$$\begin{aligned} i_{0,\text{int},i} = i_{0,\text{ref}}^{\text{int}} \left(\frac{c_{s,i}^{\text{max}} - c_{s,i}^{\text{surf}}}{c_{\text{ref}}} \right)^{\alpha} \left(\frac{c_{s,i}^{\text{surf}}}{c_{\text{ref}}} \right)^{\alpha} \left(\frac{c_{e,i}}{c_{\text{ref}}} \right)^{\alpha} \\ \exp \left[\frac{E_a^{\text{int}}}{R} \left(\frac{1}{T_{\text{ref}}} - \frac{1}{T} \right) \right] \end{aligned} \quad [21]$$

where $i_{0,\text{ref}}^{\text{int}}$ is the exchange current density of the intercalation reaction at the reference concentration of c_{ref} , c_s^{max} is the maximum solid-phase concentration, c_s^{surf} is the solid-phase concentration at

the particle surface, and E_a^{int} is the activation energy of the intercalation reaction. Surface overpotentials for negative and positive electrodes are given by:

$$\eta_{\text{int},N} = \varphi_{s,N} - \varphi_{e,N} - Fj_N R_{\text{film}} - U_{\text{int},N} \quad [22]$$

$$\eta_{\text{int},P} = \varphi_{s,P} - \varphi_{e,P} - U_{\text{int},P} \quad [23]$$

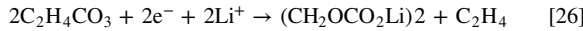
where U_{int} is the equilibrium potential for the intercalation reaction vs Li^+/Li . The total local current density for the negative electrode is the sum of the current density of three reactions: intercalation reaction, SEI reaction, and lithium plating.²⁸

$$j_N = j_{\text{int},N} + j_{\text{SEI}} + j_{\text{Li}} \quad [24]$$

Note that for the positive electrode there is only an intercalation reaction

$$j_P = j_{\text{int},P} \quad [25]$$

The SEI layer is formed due to the reduction of the electrolyte (ethylene carbonate, EC) according to the following assumed reaction²⁸



The rate of SEI formation is considered to be a function of electrolyte diffusion rate and surface kinetics according to Safari et al.³⁷ and Yang et al.²⁸ Consistent with this prior work, the local current density of SEI formation reaction is expressed here as a cathodic Tafel expression:

$$j_{\text{SEI}} = -k_{0,\text{SEI}} C_{\text{EC}}^s \exp\left(-\frac{\alpha_{c,\text{SEI}} F \eta_{\text{SEI}}}{RT}\right) \quad [27]$$

where $\alpha_{c,\text{SEI}}$ is the transfer coefficient for the SEI reaction, and the surface overpotential of SEI reaction is defined as:

$$\eta_{\text{SEI}} = \varphi_{s,N} - \varphi_{e,N} - Fj_N R_{\text{film}} - U_{\text{SEI}} \quad [28]$$

The concentration of EC on the surface of graphite is calculated based on the mass conservation of EC

$$-D_{\text{EC}} \frac{C_{\text{EC}}^s - C_{\text{EC}}^0}{\delta_{\text{Film}}} = -j_{\text{SEI}} \quad [29]$$

Temperature dependency of the SEI reaction rate constant is considered as an Arrhenius behavior²⁹

$$k_{0,\text{SEI}} = k_{0,\text{ref}}^{\text{SEI}} \exp\left[\frac{E_a^{\text{SEI}}}{R} \left(\frac{1}{T_{\text{ref}}} - \frac{1}{T}\right)\right] \quad [30]$$

where E_a^{SEI} is the activation energy for the SEI reaction. The rate of lithium deposition reaction is given by a truncated (irreversible) Butler-Volmer equation as proposed in the literature.^{42,43}

$$j_{\text{Li}} = \begin{cases} \frac{i_{0,\text{Li}}}{F} \left[\exp\left(\frac{\alpha_{a,\text{Li}} F \eta_{\text{Li}}}{RT}\right) - \exp\left(-\frac{\alpha_{c,\text{Li}} F \eta_{\text{Li}}}{RT}\right) \right], & \eta_{\text{Li}} < 0 \\ 0, & \eta_{\text{Li}} \geq 0 \end{cases} \quad [31]$$

$$\eta_{\text{Li}} = \varphi_{s,N} - \varphi_{e,N} - Fj_N R_{\text{film}} \quad [32]$$

$$i_{0,\text{Li}} = i_{0,\text{ref}}^{\text{Li}} \left(\frac{c_{e,N}}{c_{\text{ref}}}\right)^{\alpha_{a,\text{Li}}} \exp\left[\frac{E_a^{\text{Li}}}{R} \left(\frac{1}{T_{\text{ref}}} - \frac{1}{T}\right)\right] \quad [33]$$

Although some fraction of the deposited Li is reversible, the reversible part does not contribute to the capacity loss and would not necessarily persist from one cycle to another. Therefore, for simplicity in this work, we assume any reversible Li-plating reaction is included in the graphite intercalation reaction and its associated Butler-Volmer equation.

The presence of SEI and lithium metal are each tracked by a material balance²⁹:

$$\frac{\partial c_{\text{SEI}}}{\partial t} = -a \frac{j_{\text{SEI}}}{2} \quad [34]$$

$$\frac{\partial c_{\text{Li}}}{\partial t} = -a j_{\text{Li}} \quad [35]$$

where, c_{SEI} and c_{Li} are respectively the molar concentration of SEI and Li metal per unit volume of the electrode. SEI and Li metal create a surface film at the interphase of graphite particle, which can be accounted for in terms of thickness:

$$\delta_{\text{Film}} = \frac{1}{a} \left(\frac{c_{\text{SEI}} M_{\text{SEI}}}{\rho_{\text{SEI}}} + \frac{c_{\text{Li}} M_{\text{Li}}}{\rho_{\text{Li}}} \right) \quad [36]$$

where M and ρ represent the molecular weight and density, respectively. The resistance associated with this film, R_{film} , is given by

$$R_{\text{film}} = \frac{c_{\text{SEI}} M_{\text{SEI}}}{a \sigma_{\text{SEI}} \rho_{\text{SEI}}} \quad [37]$$

where σ_{SEI} is the electronic conductivity of the SEI film. Electrode porosity is reduced with increasing film thickness according to

$$\frac{d\epsilon}{dt} = -\beta a \frac{d\delta_{\text{Film}}}{dt} \quad [38]$$

β is the fraction of side-reaction products (SEI+plating) that volumetrically fill the anode pores. Two factors cause β to be less than 1. First, a portion of the side-reaction products is formed between the anode and separator and therefore does not contribute substantially to pore filling. Second, experimental imaging suggests that products accumulating in the pores do so as a nanoporous solid phase. Therefore, $\beta = 0.25$ is taken to represent these observed conditions. The overall capacity loss is calculated from both accumulated Li plating and SEI formation:

$$q_{\text{Loss}} = Fa \int_{x=0}^{L_N} \int_{t=0}^t (j_{\text{Li}} + j_{\text{SEI}}) dt dx \quad [39]$$

Parallel region model and solution.—A finite-element-based commercial package, COMSOL Multiphysics 5.3, was used to solve the above model equations. The primary dependent variables are φ_s , φ_e , c_s , c_e , c_{SEI} , c_{Li} , and T . Except c_s , which is defined in 2D, the other variables are defined in 1D. The generated mesh for the pseudo-2D particle geometry consisted of 98 quadrilateral elements and the 1D geometry included 60 elements. Further refinement of the mesh had no significant impact on the results. The equations at each timestep are solved using a direct solver called MUMPS, which utilizes LU decomposition.

As mentioned earlier, a parallel-region-model approach developed previously in our group³¹ is used to address electrode heterogeneity. In this approach, a system of three regions is connected in parallel, each of which has a certain internal ionic

resistance indicated as high, medium, or low regions in Fig. 1a. As shown in Fig. 1b, an equivalent circuit for this system consists of three parallel resistances, where the voltage for each region is the cell voltage and the total cell current is the sum of the three region currents. This follows from the fact that each region is connected to the same current collector. The portion of the current flowing in each region is inversely proportional to its resistance and is determined by a controller function added to the model.

As shown in Fig. 1c, a similar equivalent circuit is used for heat transport. The prior parallel-region model assumed independent temperatures in each region, allowing one region to be at a different temperature than the others depending on local current densities. However, subsequent consideration of the high thermal conductivity of the metallic current collectors suggests that regions separated by a few mm lateral distance rapidly equilibrate thermally in this direction through the current collectors. Hence, in the current model, thermal equilibrium is allowed by modifying the heat balance external boundary conditions one would use for a single region Eqs. 18 and 19 to become:

$$-N \frac{\partial T_{N,s}}{\partial x} \Big|_{x=0} = h(T_\infty - T_{N,s}) + h'(T_{N,s'} - T_{N,s}) + h'(T_{N,s''} - T_{N,s}) \quad [40]$$

$$-P \frac{\partial T_{P,s}}{\partial x} \Big|_{x=L_N+L_S+L_P} = h(T_{P,s} - T_\infty) + h'(T_{P,s} - T_{P,s'}) + h'(T_{P,s} - T_{P,s''}) \quad [41]$$

where s , s' , and s'' denote each region and its two neighboring regions in the respective positive or negative electrode. h' is an effective heat transfer coefficient that accounts for the large conductivity through the current collector. As such, $h' \gg h$ is a sufficient condition to equilibrate temperature between regions while maintaining numerical stability; a physically exact value of h' is not required in the model. Indeed, the same value of h' is used for both aluminum and copper current collectors for simplicity.

As mentioned above, in the parallel-region model, three different regions in the electrode are considered to represent mesoscale

heterogeneity in tortuosity in a real battery electrode. Each region has a specific tortuosity and porosity associated with it, namely a “high” region with high tortuosity and low porosity, a “low” region with low tortuosity and high porosity, and a “medium” region with moderate tortuosity and porosity. Tortuosity and porosity values for the medium region are the same as the base model parameters obtained from the experimental measurement. Table 3 lists the value of these parameters assigned for high and low regions.

A full P2D electrochemical model runs for each region separately. Thus, we assume that the three regions communicate with each other only through the current collector, namely by allowing electrical current and heat to distribute between regions. To ensure the equality of potentials between regions in anode and cathode, the solid potential at the anode current collector is grounded as mentioned in Eq. 9.

Lateral heterogeneity in electronic resistance on mm length scales is known to exist but has a relatively small effect compared to corresponding ionic transport heterogeneity and therefore is not considered in our model due to its negligible impact on Li plating.⁴⁵ Note that for graphite and all practical cathode materials, average ionic conductivity is considerably less than electronic conductivity. For instance, according to our measurements for graphite, the effective electronic conductivity is about 380 times greater than the effective ionic conductivity (27.9 vs 0.073 S m⁻¹) for reference electrolyte and temperature. A consequence of this disparity is that heterogeneity in electronic conductivity is much less likely to impact cell behavior.

In most of the cases considered in this work, we further assume that active materials are distributed uniformly across the electrode. That is, electrode heterogeneity only arises from the non-uniform distribution of carbon, binder, and pores, which leads to non-uniformity in electrode tortuosity. This assumption is supported by previous observations of active material, carbon, and binder domain in SEM/FIB images of different regions in an electrode.³¹ According to Mistry et al.,²⁴ non-uniform active material loading can also exist in the lateral direction. Hence, in a second case, we assume that active material particles are not distributed uniformly at the same time as the non-uniform distribution of pore structure.

A focus of this effort is to examine the effects of the lateral heterogeneity in the electrode that has been shown to exist on a scale

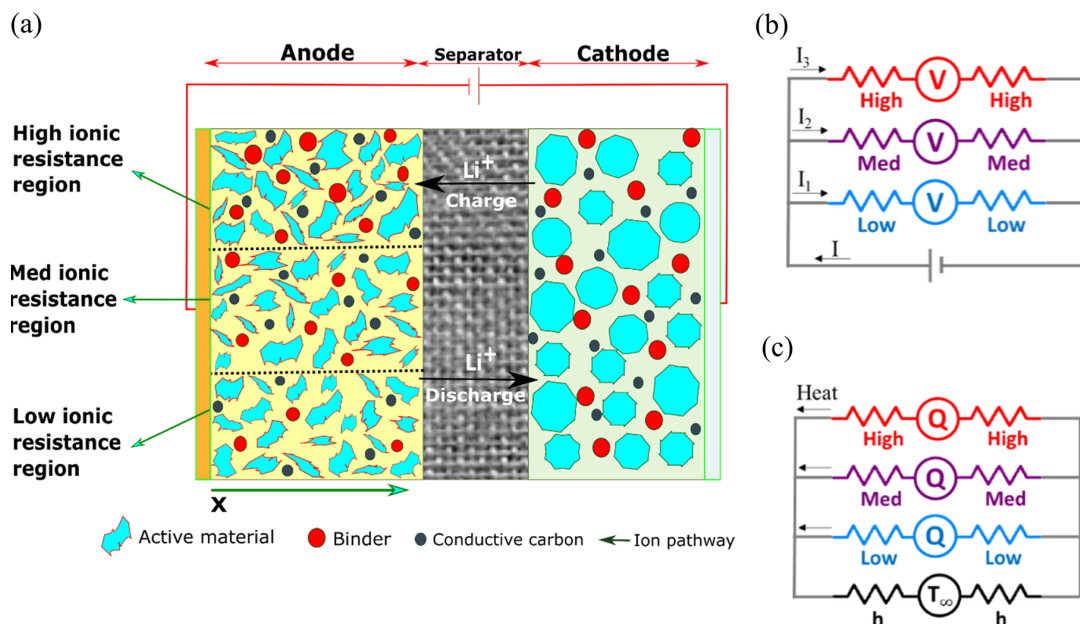


Figure 1. (a) schematic of Li-ion battery with three regions for different ionic resistances in the anode. (b) Electrical and (c) thermal equivalent circuit models. V and Q represent cell voltage and heat generation, respectively.

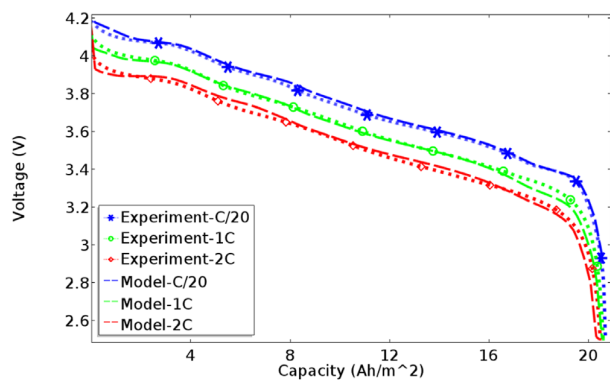


Figure 2. Cell potential comparison for simulation (line) and experimental data (symbol) for the 18650 cell at different C-rates.

of a few hundred micrometers and even to larger distances.^{31,32} This scale is greater than the electrode thickness; therefore, electrodes were considered initially homogenous in the through-plane direction. We further assume that the surface area fraction for the three regions is equal, which is equivalent to separating a continuous probability distribution (in this case for tortuosity) into three equal-sized bins. This is meant to generate and illustrate heterogeneous results even if the details of the distribution are somewhat coarse-grained. Furthermore, ionic transport in the in-plane directions between the three regions is neglected, due to the assumed large lateral scale of the heterogeneity compared to film thickness.

Experimental Method

Measurements were made from a combination of tests on 18650 cells and coin cells and pouch cells made from electrode materials harvested from the 18650 cells. The 18650 cells were commercially available 2-Ah graphite/LiNiCoAlO₂ (NCA) cells made by Samsung. To harvest electrode materials, a fresh cell was discharged to 0% SOC, then the two ends of the metallic can were carefully cut open without damaging the jellyroll or causing a short circuit. Then, the jellyroll was removed from the can and unrolled and cut.

Coin cells and pouch cells were made using the harvested electrodes, a separator (Celgard 3501, Celgard LLC, Charlotte, NC), and an electrolyte solution of 1 M lithium hexafluorophosphate in a 50/50 (v/v) mixture of ethylene carbonate and diethyl carbonate (Sigma Aldrich) in an argon atmosphere glovebox (moisture content 0.9 ppm and oxygen content < 2 ppm, VAC, Hawthorne, CA). Pouch half cells were made from the harvested electrodes paired with lithium metal pressed onto a copper current collector. After completing formation cycles at 0.05 C-rate at 24 °C, the coin cells and pouch cells were cycled at various charging C-rates (1 C, 2 C, 3 C, and 5 C). Pouch half-cell open-circuit potentials (OCP) were measured at a C/20 rate at 24 °C and -10 °C. The cycling tests were carried out using a Maccor 4300 battery cycler according to the following procedure: charge at the specified constant current to a cutoff voltage followed by a constant voltage step to 0.05 C; then discharge at 1 C constant current to a cutoff voltage followed by a constant voltage step to 0.05 C. The respective cutoff voltages were

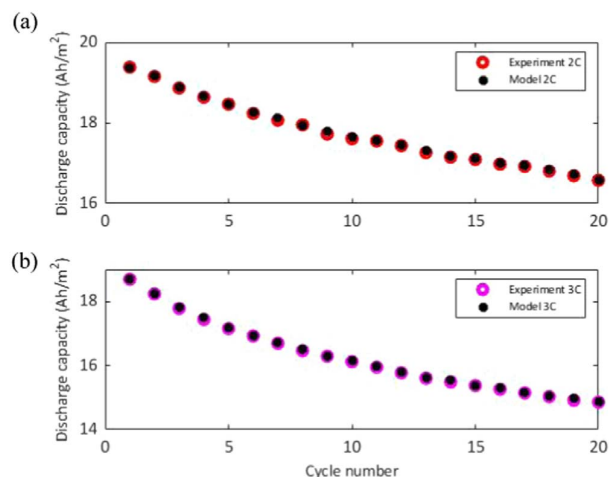


Figure 3. Model fit and experimental discharge capacity data for coin cell cycled at (a) 2 C and (b) 3 C rate charge.

4.2 V and 2.5 V for full cells and cathode half cells, and 1.5 V and 0.05 V for graphite half cells.

Results and Discussion

The base P2D model parameterization and validation.— Multiple baseline parameters were obtained by comparing model results and experiments. Half-cell experiments were used to find the OCP and operating windows of electrodes to use in the P2D model. The value of intercalation exchange current density and solid-phase diffusivity for both positive and negative electrodes were adjusted to find the best match between the experimental results and the model prediction. Figure 2 shows both simulated and experimental results for discharge curves, which agree reasonably well.

Two sets of experiments were conducted to obtain two possible values of rate constant $i_{0, \text{ref}}^{\text{Li}}$ for lithium plating. First, the 18650 cell was cycled at 0 °C to create an aggressive cycling condition and promote the Li-plating reaction. Nevertheless, the amount of capacity loss was not substantial and there was not a visible sign of Li plating on the surface of graphite after disassembly. While this is admirable for purposes of a well-functioning cell, it made it difficult to analyze the lithium metal formation. Hence, additional experiments were conducted with coin cells cycled at 24 °C, where a significant capacity loss and Li plating were observed. The summary of fast-charge experiments is presented in Table IV.

Figure 3 shows the model fit for the discharge capacity during cycling for coin cells cycled at 2 C and 3 C charge rate, where the Li-plating reaction rate constant was adjusted to match the discharge capacity.

In order to obtain the exchange current density for SEI and Li-plating reaction, we assumed the amount of capacity loss due to Li plating was much higher than the capacity loss due to SEI. This is a reasonable assumption since capacity loss due to SEI is more significant at higher temperatures or longer-term cycling.²⁷ Moreover, SEI formation does not generally result in a rapid capacity decline. When rapid decline is observed, and post-mortem

Table IV. Summary of cell type and operating conditions for Li-plating experiments.

Cell type	Operating conditions	Lithium plating
18650	0 °C, 24 °C 2 C charge rate	No significant plating observed
Pouch/coin cell	24 °C 1 C, 2 C, 3 C charge rates	Significant plating observed

analysis reveals Li plating, Li plating can be considered as the dominant mechanism.⁴⁶ Hence the lower value assigned to $i_{0,ref}^{SEI}$ compared to $i_{0,ref}^{Li}$. (It is important to recognize that each reaction is concentration-, potential-, and temperature-dependent and so actual local current densities do not depend solely on $i_{0,ref}$ values).

Local lithium plating.—An exemplary 18650 cell and its associated coin and pouch cells were cycled to investigate Li-plating behavior. The 18650 cell was disassembled after 50 cycles (2C-rate and 0 °C), and it did not show any visible sign of Li plating at the surface of the anode. However, coin cells and pouch cells cycled at different C-rates showed more severe capacity loss and had significant Li deposition on the surface of the anodes (Fig. 4a). Photographs of the anodes of these pouch cells accompanied by their segmented images are shown in Fig. 4b, where the white color represents the area with obvious Li plating. Li plating on the surface of the anode is visible as a distinct region and the area of this region increases with increasing C-rate. These pouch cells were disassembled at the charged state where graphite has a yellow color due to the formation of LiC₆.

As mentioned above, pouch or coin cells compared to the 18650 cell showed more capacity loss and Li plating at a similar C-rate. This difference could have arisen from different sources. Different electrolytes were used; possibly electrolyte in the 18650 cell included additives that could suppress Li plating. Assembly conditions were also different; for instance, a degassing step would be expected for the 18650 cell. Cell format could also be an effect: the metal can of the 18650 cell led to simultaneously much higher stack pressure and, compared to pouch cells, a better seal. Stack pressure could have a beneficial effect on suppressing inactive Li metal formation as suggested by Louli et al. work on anode-free cells.⁴⁷ Lastly, electrodes of the pouch and coin cells were harvested from a 18650 cell so they may have some additional degradation as opposed to the relatively pristine electrodes in the 18650 cell. For instance, despite gentle handling, the original SEI may experience changes during the harvesting process. To counteract this, two formation cycles were conducted on the pouch and coin cells following their assembly.

The acceleration of Li plating for our pouch and coin cells led to a larger $i_{0,ref}^{Li}$ value for these cells than for the 18650 cell. We chose to use the larger parameter for subsequent cell simulations since it showed the Li plating earlier and so eliminated the need for cycling the model as long to see the effects. Even for 20 cycles, the model requires substantial computational time on a desktop computer.

(Thus, the use of the larger kinetic parameter can be considered as a type of accelerated life testing.) Nevertheless, for modeling analysis of a well-designed cell, a substantially smaller $i_{0,ref}^{Li}$ value can be used than what is given in Table II. To wit, when applying the present model to other cells, a unique $i_{0,ref}^{Li}$ value particular to a cell can be determined by matching the experimental discharge capacity under cycling conditions likely to cause lithium plating. Furthermore, improved experimental quantification of the actual amount of inactive Li metal formed could inform the estimation of this parameter.⁴⁸

Scanning electron microscope (SEM) images were taken from the surface of a pouch cell anode with Li deposition (interior of the white area in Fig. 4b). As shown in Fig. 5, Li-plating heterogeneity was observed with spacing on the order of a few hundreds of micrometers. Heterogeneous electrodes with areas of locally high ionic resistance can exacerbate the effect of mass-transfer limitations, especially at high charge C-rates. Although the underlying cause of localized Li plating can be more complex, we postulate that localized Li plating is accelerated when electrode heterogeneity is accompanied by other factors that can promote Li plating such as edge effects,^{49,50} uneven pressure,⁵¹ or temperature, and potential gradients across large electrode distances.

After parameterizing our model with experimental cell data, we then used it to investigate the effect of electrode heterogeneity on the extent of localized Li plating.

Heterogeneity modeling study.—Lateral heterogeneity may exist in both cathode and anode coatings. In this study, we consider four different cases to investigate its effect on lithium plating. For the first two cases, we consider both anode and cathode to consist of three different resistance regions. For case one, the three regions are aligned, meaning the high-resistance region of the anode or high MacMullin number (N_M) is facing the high-resistance region of the cathode and so on, which represents the most extreme case of heterogeneity in a cell. For the second case, three regions are misaligned, meaning the high-resistance region of the anode is facing the low-resistance region of the cathode, and so on. For the third case the cathode is heterogeneous (consisting of three different regions); however, the anode is made uniform meaning all three regions have identical base-level properties. And finally, for the fourth case, a uniform cathode is coupled with a heterogeneous anode. The purpose of the two latter cases is to investigate the separate contribution of each electrode's heterogeneity on Li plating when the active material content is distributed equally in all regions.

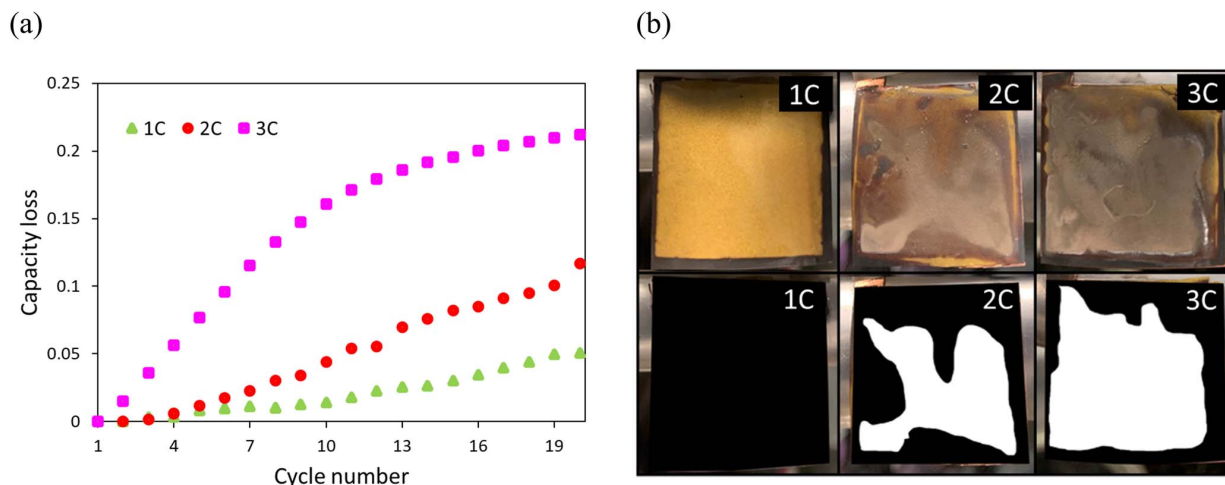


Figure 4. (a) Capacity loss as a fraction of the initial capacity vs cycle number data for pouch cells respectively cycled at 1 C, 2 C, and 3 C charge C-rates and at 24 °C. (b) Photographs of disassembled charged anodes (top) and corresponding segmented images (bottom) in which the white area represents regions with obvious lithium deposition.

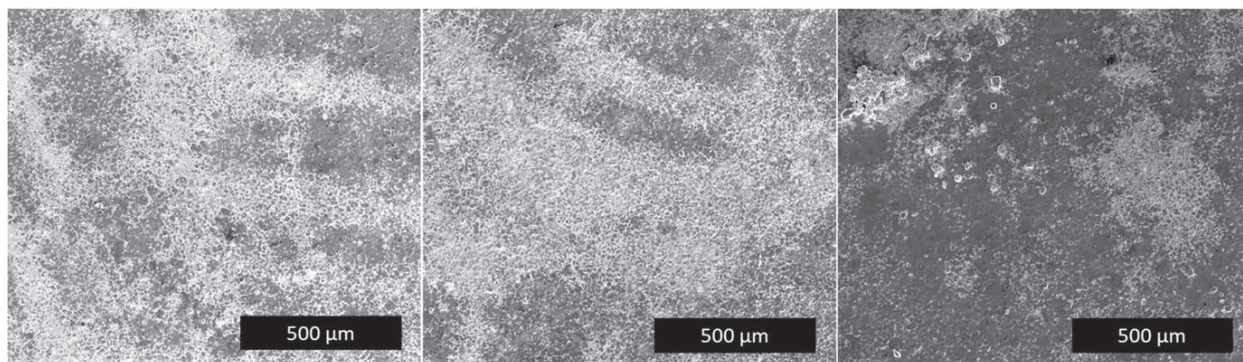


Figure 5. SEM images of the surface of the graphite anode (pouch cells) with lithium deposition, showing non-uniform lithium deposition on the surface of the anode.

Summary of case studies is presented in Table V. An additional case study 5 is also considered which is discussed in the next section.

For the first case (Fig. 6a) in which heterogeneity existed in both electrodes (aligned), there is a significant difference in local capacity loss between the regions. This observation suggests that the region with high ionic resistance is more prone to Li plating. For the second case (Fig. 6b), the difference between regions is almost the same as in the first case, suggesting the regions' alignment or misalignment does not affect Li plating.

The third case (Fig. 6c) where the anode was chosen to be uniform leads to a more uniform distribution of Li plating and capacity loss in the three regions. This clearly indicates that cathode uniformity does not have a significant effect on reducing non-uniformity in Li plating and local capacity loss, at least for the coating porosity and thickness values used here. For the last case (Fig. 6d) in which the cathode was chosen to be uniform, there is still a significant non-uniformity in the capacity loss that is similar to the case where both electrodes were heterogeneous. Moreover, this result clearly shows the significance of anode microstructure uniformity for delaying the Li-plating onset. Or from another standpoint, to have a more accurate prediction of Li-plating onset, it is necessary to account for the heterogeneity in the negative electrode in the electrochemical model.

Figure 6 also shows the Li-plating thickness of the three parallel regions as a function of anode depth, where plating is assumed to be a uniform coating on all active particles at a particular electrode depth. Li plating is more severe as expected in the high-tortuosity region and the low region has the lowest amount. For all regions, the highest Li-plating amount is at the separator interface and continually decreases until it is negligible at around 80% depth of the anode.

Li-deposit growth reduces the porosity within that volume. This result suggests that even though we assumed initial uniform tortuosity and porosity in the through-plane direction, allowing the porosity to change over time in this direction leads to heterogeneity in the through-plane direction besides heterogeneity in the lateral direction. Figure 7 shows SEM images of the cycled anode at a 3 C charge rate, confirming this concept. Li plating is observable in the pores at higher amounts near the separator region of the electrode.

It should be mentioned that Li plating in a real cell can grow off the surface of the anode into a space between the anode and separator, pushing up the separator or even penetrating through the separator. Such plating is observed in Fig. 7. However, such a mechanism is not included in our model. Essentially there is no failure mechanism in this model that causes Li dendrites to extend beyond the vicinity of graphite active material. The progressive heterogeneity in the through-plane direction can cause the evolution of a feedback mechanism that is discussed later.

Figure 8 shows the voltage-capacity and temperature profiles of the three regions for an initial 2 C charge and 1 C discharge cycle when only the anode is heterogeneous. The voltage profiles of the three regions are comparable, with slight differences in state of charge at the end of discharge, meaning that higher tortuosity results in slightly lower effective capacity. The temperature profile of the three regions is expected to overlap due to the common temperature at the current collectors. Temperatures at the interior of each region are allowed to differ, but as shown in Fig. 8b, do not. This confirms that thermal communication between the regions via the common current collectors is relatively high. The largest observed temperature rise occurs during the relatively fast constant-current charging step, indicating this is the time most susceptible to thermally induced damage to cell materials.

Feedback mechanism between heterogeneous regions.—As mentioned above, the effect of a heterogeneous cathode on lithium plating is negligible, therefore, to study the feedback mechanisms between heterogeneous regions, only the heterogeneous anode is considered in this section.

As shown in Table VI, an additional case was studied and is compared to the most similar previous case. In case four, all three regions have the same active material content while in case five, regions have different active material loading while the filler volume fraction between regions is the same. The porosity and tortuosity of the regions are similar to that of the fourth case.

The three-region model was run for the fourth and fifth cases at a 2 C charge 1 C discharge rate at 24 °C for 25 cycles. Capacity loss is the amount of SEI and inactive plated lithium divided by the corresponding amount of cyclable lithium at initial cell capacity. It

Table V. Heterogeneity in five case studies.

Case studies	Heterogeneity
Case 1	Heterogeneous ionic transport, anode, and cathode, aligned regions
Case 2	Heterogeneous ionic transport, anode, and cathode, misaligned regions
Case 3	Heterogeneous ionic transport, cathode only
Case 4	Heterogeneous ionic transport, anode only
Case 5	Heterogeneous ionic transport and active material loading, anode only

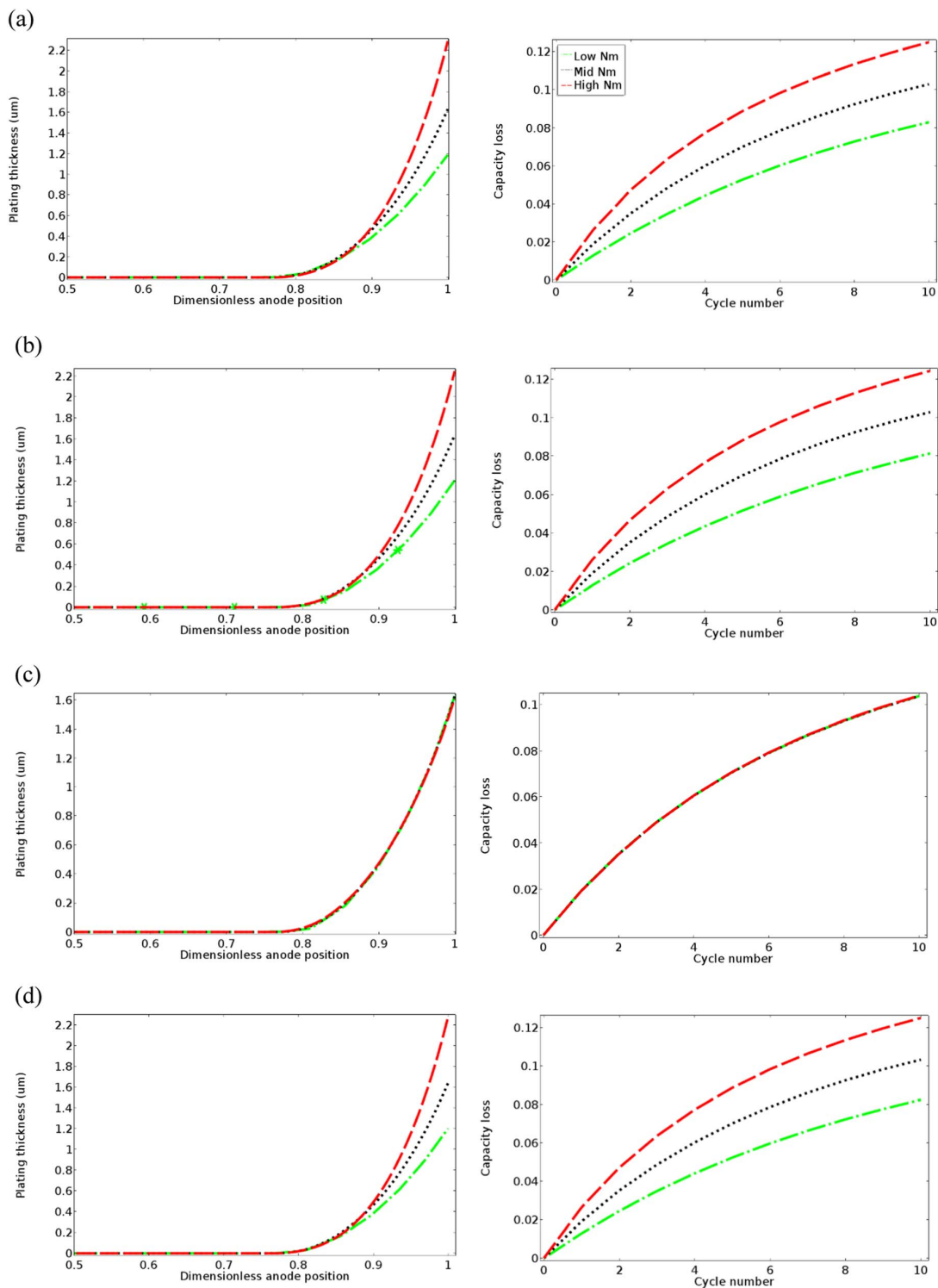


Figure 6. Simulated plating thickness and capacity loss and for 2 C charge and 1 C discharge for four cases: (a) both anode and cathode are heterogeneous (aligned), (b) both anode and cathode are heterogeneous (misaligned), (c) a heterogeneous cathode is coupled with a uniform anode, (d) a heterogeneous anode is coupled with a uniform cathode. Discrete points calculated at the end of each cycle were connected to form smooth curves.

should be noted that in the fifth case, the areal capacity of each region was weighted by the active material loading in that region.

According to Fig. 9a, the region with the highest MacMullin number always exhibits the highest capacity loss when regions have

the same active material loading (case four). This region’s capacity loss further diverges from the other regions around cycle 15 because of the feedback from the filling of pores near the separator. In other words, the high N_M region reaches the end of life much sooner than

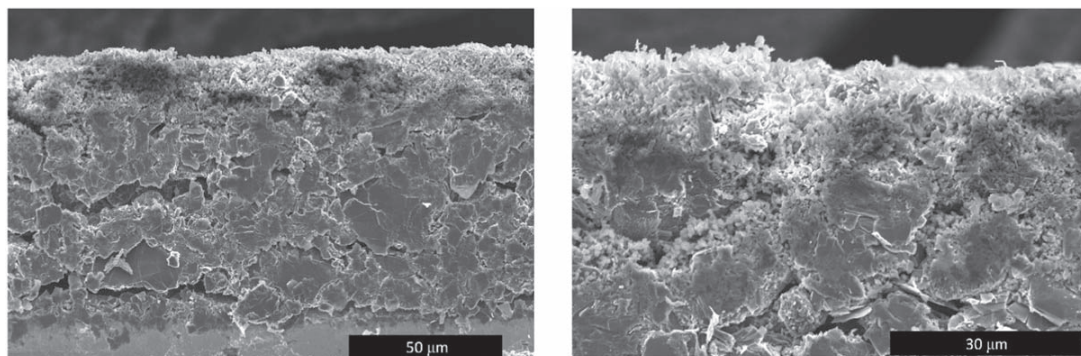


Figure 7. SEM-FIB cross-sections of anode after 3C-charge cycling. Two different locations with their magnifications are shown. The current collector is on the bottom and the separator is on top. Lithium dendrites are clear near the separator interface. In the image on the right, Li dendrites are shown to fill anode pores near the separator.

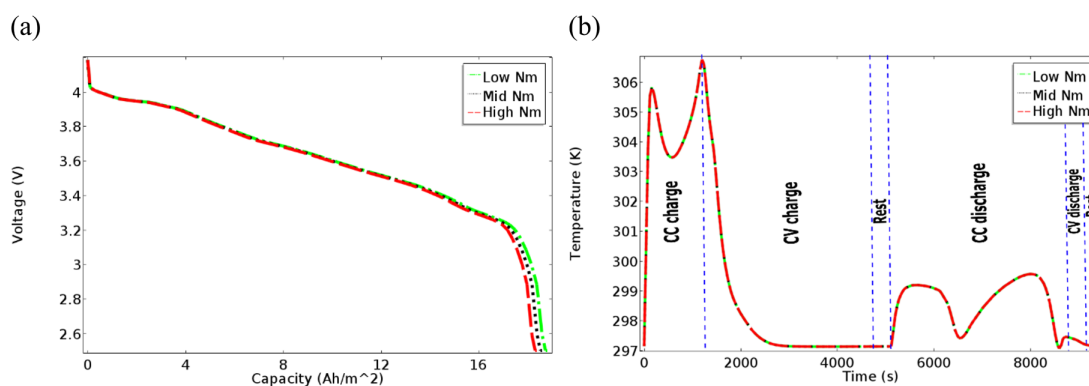


Figure 8. Simulated discharge voltages (a) and temperature profiles (b) of three regions for a 2 C charge and 1 C discharge cycle. The temperatures are probed at the anode-separator interface.

Table VI. The anode parameters for the two cases with different active material loading.

Parameter	Low region	Medium region	High region	
Case four	ϵ_N	0.36	0.34	0.32
	ϵ_f	0.035	0.055	0.075
	τ_N	4.4	5.5	6.6
	N_M	12.2	16.2	20.6
Case five	ϵ_N	0.36	0.34	0.32
	ϵ_f	0.055	0.055	0.055
	τ_N	4.4	5.5	6.6
	N_M	12.2	16.2	20.6

the other two regions. In the fifth case, the low N_M region has the lowest active material loading and holds the highest capacity loss until cycle 20. However, the high N_M region catches up at cycle 20 and the same accelerated aging trend is observed as in case four. Additional differences are observed between cases four and five: the capacity loss of regions is more uniform in case five compared to case four, and while the Mid- N_M region ages at the same rate in both cases, the average capacity loss in case five is higher than in the case four.

It is useful to examine conditions in the two cases as the end of life is approached. End of life for case four is taken to be the point where porosity reaches zero in the high- N_M region. Figure 10a shows plating thickness across the anode at this time for both cases four and five. It is worth noting that in case five (the solid lines),

there is a crossover point, meaning the most plating at a particular depth is not always in the same lateral region. This is the main reason for higher capacity loss for the low- N_M region in case five as discussed in Fig. 9.

Li-deposit growth near the separator region reduces the porosity within that volume as depicted in Fig. 10b. As with previously examined cases, a model that allows the porosity to change over time can lead to heterogeneity in the through-plane direction besides heterogeneity in the lateral direction. Figure 10b shows that for case five plating penetrates to a greater depth of anode in the low- N_M region (about 28% of depth) while in the fourth case, all regions have almost the same plating penetration depth (about 20% of depth). This heterogeneity in the through-plane direction can cause the feedback mechanism in the high- N_M region causing the accelerated capacity decay shown in Fig. 9.

This feedback mechanism also affects the current distribution between regions during cycling. In the first cycle (Fig. 11a), a more uniform current distribution is observed between regions in both cases, while in cycle 13 (Fig. 11b) the current distribution in case four becomes less uniform. The low N_M region gains a higher current for almost the whole time during cycle 13 when different regions have the same active material loading (case four). The reason for this happening can be traced to Fig. 10b where the ionic resistance of the high- N_M region is increased due to pore blockage near the separator interface compared to the other two regions. For case five, the current density distribution for cycle 13 follows almost the same trend as for the first cycle.

A closer look into the Li-plating overpotential can help us to investigate the difference in the total capacity loss for the two case studies. The change in the slope of Li-plating overpotential near the

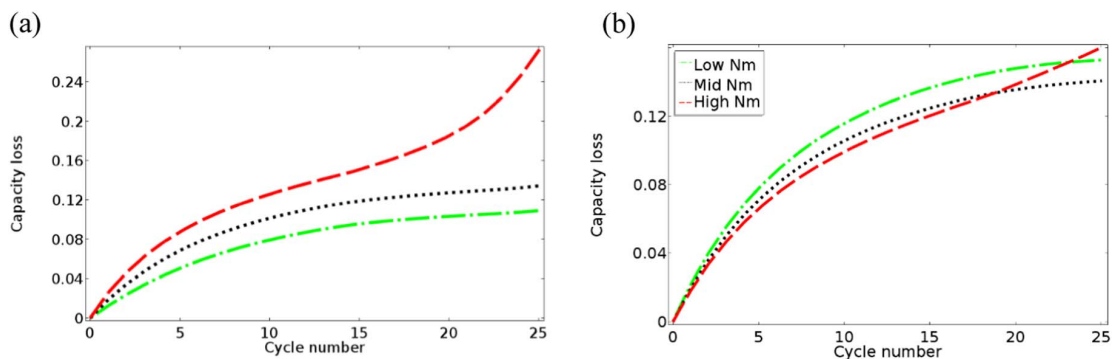


Figure 9. Capacity loss (a) for case four where all regions have the same active material fractions, (b) case five where regions have different active material fractions.

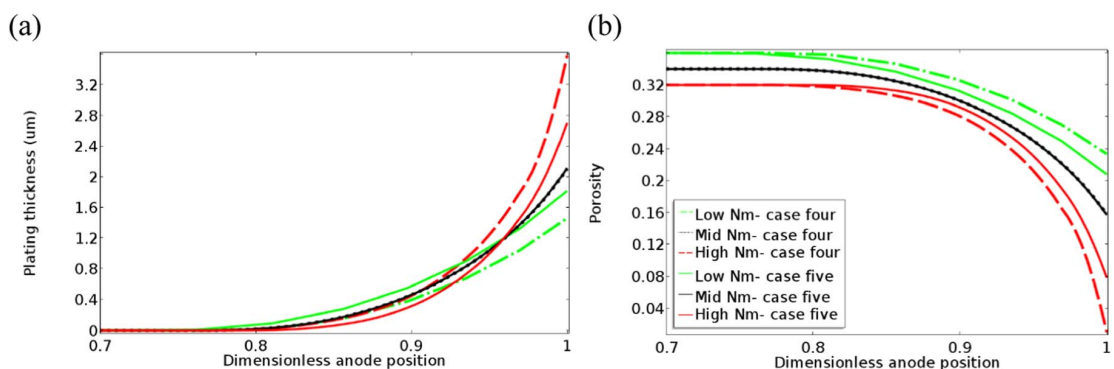


Figure 10. (a) plating thickness, and (b) anode porosity vs anode depth for three parallel regions and study cases four and five. Plots are at cycle 13, which is effectively the end of life for case four.

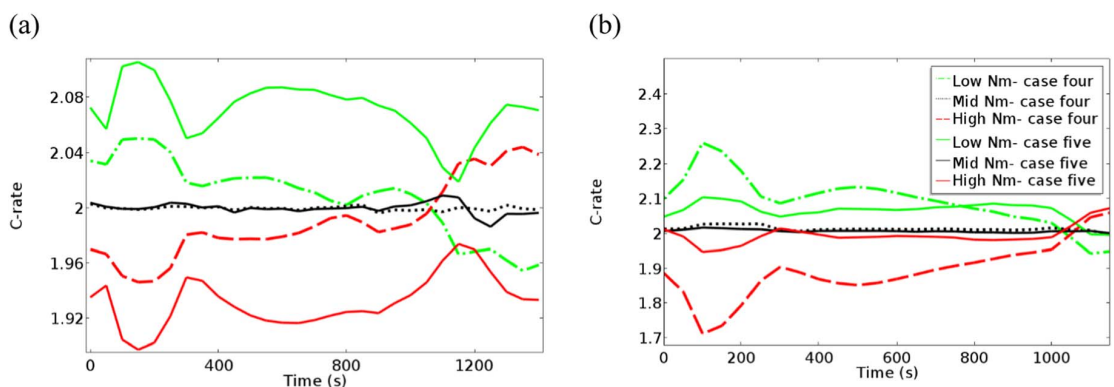


Figure 11. Current density distribution between regions (in terms of C-rate) at the anode-separator interface during the constant current charge for study cases four (dashed lines) and five (solid lines), at (a) first cycle and (b) cycle 13. Vertical axes are at different scales.

separator (Fig. 12a) is due to the SEI resistance which inhibits further Li plating (last term in (32)). In the absence of this term, Li-plating overpotential would follow a smooth trend as suggested by the curve of electrolyte potential shown in Fig. 12b. As mentioned above, although all regions have an increase in plating as one approaches the separator, there are differences in which regions experience the highest amount of plating at a given depth. Furthermore, the degree of heterogeneity, as indicated by the differences between plating overpotential of the high- N_M and low- N_M regions, is greater for case five than case four. More specifically, the depth at which Li plating is possible is more heterogeneous for case five.

Figure 13 focuses on the low- N_M region to understand the difference in plating trends observed in cases four and five. Figure 13a illustrates that the low- N_M region in case five always displays lower plating overpotential than in case four i.e., it is more susceptible to lithium plating. This stems from the higher surface concentrations of particles in case five due to lower active material loading (Fig. 13b). This excess surface concentration makes the particles prone to Li plating. However, at the end of cycling, more Li plating forms in the high- N_M region due to the positive feedback from clogged pores as shown in Fig. 9b.

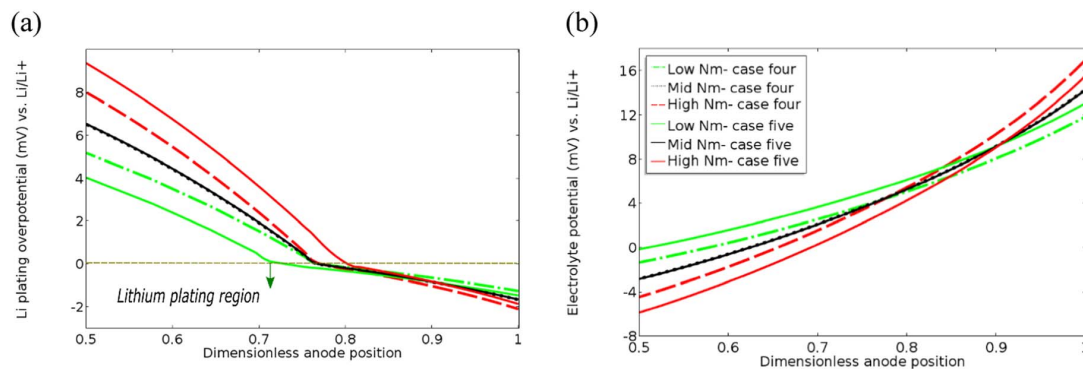


Figure 12. (a) Li-plating overpotential, and (b) electrolyte potential with anode depth at the end of the constant current charge of the first cycle for three regions and cases four and five.

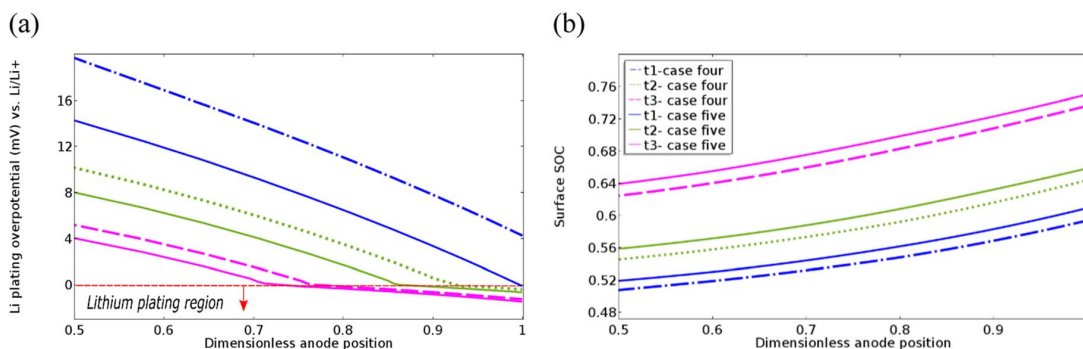


Figure 13 . (a) Li-plating overpotential, and (b) particle surface state of charge (SOC) at three different times near the end of constant current charging ($t_1 = 1100$ s, $t_2 = 1250$ s, $t_3 = 1400$ s) as a function of anode depth for study cases four and five.

Conclusions

In order to reduce the degree of Li plating in a cell, it is necessary to understand the root causes. This work examines the interplay of electrode heterogeneity and Li plating by utilizing a parallel-region model that combines three Newman-type submodels and an equivalent-circuit controller. A prior model using this same principle was extended by incorporating irreversible SEI and Li-plating reactions. The three parallel regions represent portions of the electrode that have, respectively, high, medium, and low ionic transport resistance. These model assumptions are valid for lateral heterogeneity in tortuosity on length scales greater than the thickness of the electrode film, meaning hundreds of micrometers or greater.

Our parallel-region model can be thought of as a reduced-order 3D model, in that it attempts to describe the most salient aspects of heterogeneity in the in-plane and through-plane directions. This allows for computations of systems and timescales that would be difficult for a fully realized 3D model. Furthermore, geometric parameterization of our model is easier than would be the case for a model that requires a 3D structure valid from μm to mm length scales.

To parameterize the model, experiments were performed for a 18650 cell and derived coin and pouch cells, under cycling conditions that promoted Li plating. Visual confirmation of plating was made for the pouch cells. The coin cells likewise made from the 18650 cell experienced enhanced capacity loss that we associated with lithium plating.

Using the model, the effect of electrode heterogeneity on Li plating was investigated first for four cases: heterogeneous anode and cathode (aligned and misaligned regions), heterogeneous cathode coupled with a uniform anode, and a heterogeneous anode coupled with a uniform cathode. In these cases, the active material loading was equally distributed among regions. The simulations

show that heterogeneity in the anode can result in non-uniform Li plating; however, cathode heterogeneity did not have a significant effect. That is, a non-uniform anode leads to more Li deposition in the higher tortuosity region, especially at higher C-rates. This difference in sensitivity to heterogeneity is caused by the cathode having a lower average MacMullin number or tortuosity than the anode. Furthermore, a positive feedback mechanism exists between the porosity of each region and the rate of side reactions. Especially at the end of life, pore-clogging near the separator can be a reason for the accelerated capacity loss and short-circuit of the cell.

Another comparison was made between two cases where the active material is uniformly and non-uniformly distributed in the parallel regions. Specifically, in case five, the local loading of active material is higher where ionic resistance is higher. Otherwise, case five has the same heterogeneity in ionic resistance as case four. Interestingly, this led to lower overall Li plating for case five. Further, case five had lower heterogeneity in Li plating by lateral location. Thus, heterogeneity in loading can compensate for heterogeneity in ionic resistance and lead to less Li-plating heterogeneity compared to a case where loading is uniform.

The modeling concept developed here is useful for any situation in which parallel regions have a dissimilar property, such as resistance, loading, temperature, or other relevant property. It has some of the descriptive advantages of a 3D model without the computational expense. The model could further be applied to cases beyond mm scale heterogeneity in one cell to include multiple parallel cells experiencing aging within a battery pack.

Acknowledgments

This material is based upon work supported by the U.S. Department of Energy, Office of Science, Vehicle Technologies Office as part of the eXtreme Fast Charge Program.

ORCID

Amir-Sina Hamed  <https://orcid.org/0000-0002-1363-7823>Mojdeh Nikpour  <https://orcid.org/0000-0001-6069-0611>

References

- M. M. Kabir and D. E. Demirocak, "Degradation mechanisms in Li-ion batteries: a state-of-the-art review." *Int. J. Energy Res.*, **41**, 1963 (2017).
- T. Waldmann, B. I. Hogg, and M. Wohlfahrt-Mehrens, "Li plating as unwanted side reaction in commercial Li-ion cells - A review." *J. Power Sources*, **384**, 107 (2018).
- A. Barre, B. Deguilhem, S. Grolleau, M. Gerard, F. Suard, and D. Riu, "A review on lithium-ion battery ageing mechanisms and estimations for automotive applications." *J. Power Sources*, **241**, 680 (2013).
- X. B. Han, L. G. Lu, Y. J. Zheng, X. N. Feng, Z. Li, J. Q. Li, and M. G. Ouyang, "A review on the key issues of the lithium ion battery degradation among the whole life cycle." *Etransportation*, **1100005** (2019).
- S. K. Heiskanen, J. Kim, and B. L. Lucht, "Generation and evolution of the solid electrolyte interphase of lithium-ion batteries." *Joule*, **3**, 2322 (2019).
- V. Agubra and J. Fergus, "Lithium ion battery anode aging mechanisms." *Materials*, **6**, 1310 (2013).
- P. Verma, P. Maire, and P. Novak, "A review of the features and analyses of the solid electrolyte interphase in Li-ion batteries." *Electrochim. Acta*, **55**, 6332 (2010).
- A. P. Wang, S. Kadam, H. Li, S. Q. Shi, and Y. Qi, "Review on modeling of the anode solid electrolyte interphase (SEI) for lithium-ion batteries." *NPJ Comput. Mater.*, **4** (2018).
- S. J. An, J. L. Li, C. Daniel, D. Mohanty, S. Nagpure, and D. L. Wood, "The state of understanding of the lithium-ion-battery graphite solid electrolyte interphase (SEI) and its relationship to formation cycling." *Carbon*, **105**, 52 (2016).
- E. Peled and S. Menkin, "Review-SEI: past, present and future." *J. Electrochem. Soc.*, **164**, A1703 (2017).
- I. D. Campbell, M. Marzook, M. Marinescu, and G. J. Offer, "How observable is lithium plating? Differential voltage analysis to identify and quantify lithium plating following fast charging of cold lithium-ion batteries." *J. Electrochem. Soc.*, **166**, A725 (2019).
- T. Ould Ely, D. Kamzabek, and D. Chakraborty, "Batteries safety: recent progress and current challenges." *Frontiers in Energy Research*, **7**, 71 (2019).
- R. V. Bugga and M. C. Smart, "Lithium plating behavior in lithium-ion cells." *ECSTrans.*, **25**, 241 (2010).
- S. S. Zhang, K. Xu, and T. R. Jow, "Study of the charging process of a LiCoO₂(2)-based Li-ion battery." *J. Power Sources*, **160**, 1349 (2006).
- J. Cannarella and C. B. Arnold, "The effects of defects on localized plating in lithium-ion batteries." *J. Electrochem. Soc.*, **162**, A1365 (2015).
- S. J. Harris and P. Lu, "Effects of inhomogeneities-nanoscale to mesoscale-on the durability of Li-Ion batteries." *J. Phys. Chem. C*, **117**, 6481 (2013).
- M. Ebner, D. W. Chung, R. E. Garcia, and V. Wood, "Tortuosity anisotropy in lithium-ion battery electrodes." *Adv. Energy Mater.*, **4**, 5 (2014).
- Y. Yang et al., "Quantification of heterogeneous degradation in li-ion batteries." *Adv. Energy Mater.*, **9**, 25 (2019).
- M. Mühlbauer, A. Schökel, M. Etter, V. Baran, and A. Senyshyn, "Probing chemical heterogeneity of Li-ion batteries by in operando high energy X-ray diffraction radiography." *J. Power Sources*, **403**, 49 (2018).
- M. Storch, J. P. Fath, J. Sieg, D. Vrankovic, C. Krupp, B. Spier, and R. Riedel, "Temperature and lithium concentration gradient caused inhomogeneous plating in large-format lithium-ion cells." *Journal of Energy Storage*, **41**, 102887 (2021).
- D. Kehrwald, P. R. Shearing, N. P. Brandon, P. K. Sinha, and S. J. Harris, "Local tortuosity inhomogeneities in a lithium battery composite electrode." *J. Electrochem. Soc.*, **158**, A1393 (2011).
- P. P. Paul, V. Thampy, C. Cao, H.-G. Steinrück, T. R. Tanim, A. R. Dunlop, E. J. Dufek, S. E. Trask, A. N. Jansen, and M. F. Toney, "Quantification of heterogeneous, irreversible lithium plating in extreme fast charging of lithium-ion batteries." *Energy Environ. Sci.*, **14**, 4979 (2021).
- H. Charalambous, D. P. Abraham, A. R. Dunlop, S. E. Trask, A. N. Jansen, T. R. Tanim, P. R. Chinnam, A. M. Colclasure, W. Xu, and A. A. Yakovenko, "Revealing causes of macroscale heterogeneity in lithium ion pouch cells via synchrotron X-ray diffraction." *J. Power Sources*, **507**, 230253 (2021).
- A. Mistry, F. L. Usseglio-Viretta, A. Colclasure, K. Smith, and P. P. Mukherjee, "Fingerprinting redox heterogeneity in electrodes during extreme fast charging." *J. Electrochem. Soc.*, **167**, 090542 (2020).
- S. J. Cooper et al., "Image based modelling of microstructural heterogeneity in LiFePO₄ electrodes for Li-ion batteries." *J. Power Sources*, **247**, 1033 (2014).
- K. Nishikawa, T. Mori, T. Nishida, Y. Fukunaka, and M. Rosso, "Li dendrite growth and Li + ionic mass transfer phenomenon." *J. Electroanal. Chem.*, **661**, 84 (2011).
- X. G. Yang and C. Y. Wang, "Understanding the trilemma of fast charging, energy density and cycle life of lithium-ion batteries." *J. Power Sources*, **402**, 489 (2018).
- X. G. Yang, Y. J. Leng, G. S. Zhang, S. H. Ge, and C. Y. Wang, "Modeling of lithium plating induced aging of lithium-ion batteries: transition from linear to nonlinear aging." *J. Power Sources*, **360**, 28 (2017).
- X. G. Yang, S. H. Ge, T. Liu, Y. J. Leng, and C. Y. Wang, "A look into the voltage plateau signal for detection and quantification of lithium plating in lithium-ion cells." *J. Power Sources*, **395**, 251 (2018).
- D. S. Ren, K. Smith, D. X. Guo, X. B. Han, X. N. Feng, L. G. Lu, M. G. Ouyang, and J. Q. Li, "Investigation of lithium plating-stripping process in li-ion batteries at low temperature using an electrochemical model." *J. Electrochem. Soc.*, **165**, A2167 (2018).
- M. M. Forouzan, B. A. Mazzeo, and D. R. Wheeler, "Modeling the effects of electrode microstructural heterogeneities on li-ion battery performance and lifetime." *J. Electrochem. Soc.*, **165**, A2127 (2018).
- J. E. Vogel, M. M. Forouzan, E. E. Hardy, S. T. Crawford, D. R. Wheeler, and B. A. Mazzeo, "Electrode microstructure controls localized electronic impedance in Li-ion batteries." *Electrochim. Acta*, **297**, 820 (2019).
- T. G. Tranter et al., "Probing heterogeneity in li-ion batteries with coupled multiscale models of electrochemistry and thermal transport using tomographic domains." *J. Electrochem. Soc.*, **167**, 11 (2020).
- J. Newman and K. E. Thomas-Alyea, *Electrochemical Systems*. (New York, NY) (Wiley) (2012).
- M. Doyle, T. F. Fuller, and J. Newman, "Modeling of galvanostatic charge and discharge of the lithium polymer insertion cell." *J. Electrochem. Soc.*, **140**, 1526 (1993).
- P. Arora, M. Doyle, and R. E. White, "Mathematical modeling of the lithium deposition overcharge reaction in lithium-ion batteries using carbon-based negative electrodes." *J. Electrochem. Soc.*, **146**, 3543 (1999).
- M. Safari, M. Morcrette, A. Teyssot, and C. Delacourt, "Multimodal physics-based aging model for life prediction of li-ion batteries." *J. Electrochem. Soc.*, **156**, A145 (2009).
- C. von Luders, J. Keil, M. Webersberger, and A. Jossen, "Modeling of lithium plating and lithium stripping in lithium-ion batteries." *J. Power Sources*, **414**, 41 (2019).
- D. Baker and M. Verbrugge, "Modeling overcharge at lithiated-graphite porous electrodes: plating and dissolution of lithium." *J. Electrochem. Soc.*, **167**, 10 (2020).
- S. Hein, T. Danner, and A. Latz, "An electrochemical model of lithium plating and stripping in lithium ion batteries." *ACS Appl. Energy Mater.*, **3**, 8519 (2020).
- M. Song and S. Y. Choe, "Fast and safe charging method suppressing side reaction and lithium deposition reaction in lithium ion battery." *J. Power Sources*, **436**, 226835 (2019).
- R. D. Perkins, A. V. Randall, X. C. Zhang, and G. L. Plett, "Controls oriented reduced order modeling of lithium deposition on overcharge." *J. Power Sources*, **209**, 318 (2012).
- H. Ge, T. Aoki, N. Ikeda, S. Suga, T. Isobe, Z. Li, Y. Tabuchi, and J. B. Zhang, "Investigating lithium plating in lithium-ion batteries at low temperatures using electrochemical model with NMR assisted parameterization." *J. Electrochem. Soc.*, **164**, A1050 (2017).
- W. B. Gu and C. Y. Wang, "Thermal-electrochemical modeling of battery systems." *J. Electrochem. Soc.*, **147**, 2910 (2000).
- F. M. Kindermann, P. J. Osswald, G. Ehlert, J. Schuster, A. Rheinfeld, and A. Jossen, "Reducing inhomogeneous current density distribution in graphite electrodes by design variation." *J. Electrochem. Soc.*, **164**, E3105 (2017).
- Q. Liu, R. Petibon, C. Du, and J. Dahn, "Effects of electrolyte additives and solvents on unwanted lithium plating in lithium-ion cells." *J. Electrochem. Soc.*, **164**, A1173 (2017).
- A. J. Louli, M. Genovese, R. Weber, S. G. Hames, E. R. Logan, and J. R. Dahn, "Exploring the impact of mechanical pressure on the performance of anode-free lithium metal cells." *J. Electrochem. Soc.*, **166**, A1291 (2019).
- E. J. McShane, A. M. Colclasure, D. E. Brown, Z. M. Konz, K. Smith, and B. D. McCloskey, "Quantification of inactive lithium and solid-electrolyte interphase species on graphite electrodes after fast charging." *ACS Energy Lett.*, **5**, 2045 (2020).
- C. Birkenmaier, B. Bitzer, M. Harzheim, A. Hintennach, and T. Schleid, "Lithium plating on graphite negative electrodes: innovative qualitative and quantitative investigation methods." *J. Electrochem. Soc.*, **162**, A2646 (2015).
- M. Tang, P. Albertus, and J. Newman, "Two-dimensional modeling of lithium deposition during cell charging." *J. Electrochem. Soc.*, **156**, A390 (2009).
- T. C. Bach, S. F. Schuster, E. Fleder, J. Muller, M. J. Brand, H. Lorrman, A. Jossen, and G. Sextl, "Nonlinear aging of cylindrical lithium-ion cells linked to heterogeneous compression." *Journal of Energy Storage*, **5**, 212 (2016).